Measurement of absolute branching fractions of inclusive semileptonic decays of charm and charmed-strange mesons

D. M. Asner, K. W. Edwards, J. Reed, A. N. Robichaud, G. Tatishvili, E. J. White, R. A. Briere, H. Vogel, P. U. E. Onyisi, J. L. Rosner, J. P. Alexander, D. G. Cassel, S. Das, R. Ehrlich, L. Fields, L. Gibbons, S. W. Gray, D. L. Hartill, B. K. Heltsley, J. M. Hunt, D. L. Kreinick, V. E. Kuznetsov, J. Ledoux, J. R. Patterson, D. Peterson, D. Riley, A. Ryd, A. J. Sadoff, X. Shi, S. Stroiney, W. M. Sun, J. Yelton, P. Rubin, N. Lowrey, S. Mehrabyan, M. Selen, J. Wiss, M. Kornicer, R. E. Mitchell, M. R. Shepherd, C. M. Tarbert, D. Besson, T. K. Pedlar, J. Xavier, D. Cronin-Hennessy, K. Y. Gao, J. Hietala, R. Poling, P. Zweber, S. Dobbs, Z. Metreveli, K. K. Seth, B. J. Y. Tan, A. Tomaradze, S. Brisbane, J. Libby, L. Martin, A. Powell, P. Spradlin, G. Wilkinson, H. Mendez, J. Y. Ge, D. H. Miller, I. P. J. Shipsey, B. Xin, G. S. Adams, D. Hu, B. Moziak, J. Napolitano, K. M. Ecklund, J. Insler, H. Muramatsu, C. S. Park, E. H. Thorndike, F. Yang, S. Ricciardi, C. Thomas, M. Artuso, S. Blusk, S. Khalil, R. Mountain, K. Randrianarivony, T. Skwarnicki, S. Stone, J. C. Wang, L. M. Zhang, G. Bonvicini, D. Cinabro, A. Lincoln, M. J. Smith, P. Zhou, J. Zhu, P. Naik, and J. Rademacker

Measurement of absolute branching fractions of inclusive semileptonic decays of charm and charmed-strange mesons

D. M. Asner,[1] K. W. Edwards,[1] J. Reed,[1] A. N. Robichaud,[1] G. Tatishvili,[1] E. J. White,[1] R. A. Briere,[2] H. Vogel,[2] P. U. E. Onyisi,[3] J. L. Rosner,[3] J. P. Alexander,[4] D. G. Cassel,[4] S. Das,[4] R. Ehrlich,[4] L. Fields,[4] L. Gibbons,[4] S. W. Gray,[4] D. L. Hartill,[4] B. K. Heltsley,[4] J. M. Hunt,[4] D. L. Kreinick,[4] V. E. Kuznetsov,[4] J. Ledoux,[4] J. R. Patterson,[4] D. Peterson,[4] D. Riley,[4] A. Ryd,[4] A. J. Sadoff,[4] X. Shi,[4] S. Stroiney,[4] W. M. Sun,[4] J. Yelton,[5] P. Rubin,[6] N. Lowrey,[7] S. Mehrabyan,[7] M. Selen,[7] J. Wiss,[7] M. Kornicer,[8] R. E. Mitchell,[8] M. R. Shepherd,[8] C. M. Tarbert,[8] D. Besson,[9] T. K. Pedlar,[10] J. Xavier,[10] D. Cronin-Hennessy,[11] K. Y. Gao,[11] J. Hietala,[11] R. Poling,[11] P. Zweber,[11] S. Dobbs,[12] Z. Metreveli,[12] K. K. Seth,[12] B. J. Y. Tan,[12] A. Tomaradze,[12] S. Brisbane,[13] J. Libby,[13] L. Martin,[13] A. Powell,[13] P. Spradlin,[13] G. Wilkinson,[13] H. Mendez,[14] J. Y. Ge,[15] D. H. Miller,[15] I. P. J. Shipsey,[15] B. Xin,[15] G. S. Adams,[16] D. Hu,[16] B. Moziak,[16] J. Napolitano,[16] K. M. Ecklund,[17] J. Insler,[18] H. Muramatsu,[18] C. S. Park,[18] E. H. Thorndike,[18] F. Yang,[18] S. Ricciardi,[19] C. Thomas,[13,19] M. Artuso,[20] S. Blusk,[20] S. Khalil,[20] R. Mountain,[20] K. Randrianarivony,[20] T. Skwarnicki,[20] S. Stone,[20] J. C. Wang,[20] L. M. Zhang,[20] G. Bonvicini,[21] D. Cinabro,[21] A. Lincoln,[21] M. J. Smith,[21] P. Zhou,[21] J. Zhu,[21] P. Naik,[22] and J. Rademacker[22]

(CLEO Collaboration)

[1]*Carleton University, Ottawa, Ontario, Canada K1S 5B6*
[2]*Carnegie Mellon University, Pittsburgh, Pennsylvania 15213, USA*
[3]*University of Chicago, Chicago, Illinois 60637, USA*
[4]*Cornell University, Ithaca, New York 14853, USA*
[5]*University of Florida, Gainesville, Florida 32611, USA*
[6]*George Mason University, Fairfax, Virginia 22030, USA*
[7]*University of Illinois, Urbana-Champaign, Illinois 61801, USA*
[8]*Indiana University, Bloomington, Indiana 47405, USA*
[9]*University of Kansas, Lawrence, Kansas 66045, USA*
[10]*Luther College, Decorah, Iowa 52101, USA*
[11]*University of Minnesota, Minneapolis, Minnesota 55455, USA*
[12]*Northwestern University, Evanston, Illinois 60208, USA*
[13]*University of Oxford, Oxford OX1 3RH, United Kingdom*
[14]*University of Puerto Rico, Mayaguez, Puerto Rico 00681*
[15]*Purdue University, West Lafayette, Indiana 47907, USA*
[16]*Rensselaer Polytechnic Institute, Troy, New York 12180, USA*
[17]*Rice University, Houston, Texas 77005, USA*
[18]*University of Rochester, Rochester, New York 14627, USA*
[19]*STFC Rutherford Appleton Laboratory, Chilton, Didcot, Oxfordshire, OX11 0QX, United Kingdom*
[20]*Syracuse University, Syracuse, New York 13244, USA*
[21]*Wayne State University, Detroit, Michigan 48202, USA*
[22]*University of Bristol, Bristol BS8 1TL, United Kingdom*

(Received 21 December 2009; revised manuscript received 22 February 2010; published 16 March 2010)

We have measured the inclusive semileptonic branching fractions of D^0, D^+, and D_s^+ mesons. For these measurements, we have used the full CLEO-c open-charm data samples, 818 pb^{-1} at $E_{\rm CM} = 3.774$ GeV, giving $D^0\bar{D}^0$ and D^+D^- events, and 602 pb^{-1} at $E_{\rm CM} = 4.170$ GeV, giving $D_s^{*\pm}D_s^{\mp}$ events. We obtain $\mathcal{B}(D^0 \to Xe^+\nu_e) = (6.46 \pm 0.09 \pm 0.11)\%$, $\mathcal{B}(D^+ \to Xe^+\nu_e) = (16.13 \pm 0.10 \pm 0.29)\%$, and $\mathcal{B}(D_s^+ \to Xe^+\nu_e) = (6.52 \pm 0.39 \pm 0.15)\%$, where the first uncertainties are statistical and the second are systematic. From these and lifetimes obtained elsewhere, we obtain the ratios of semileptonic decay widths $\Gamma(D^+ \to Xe^+\nu_e)/\Gamma(D^0 \to Xe^+\nu_e) = 0.985 \pm 0.015 \pm 0.024$ and $\Gamma(D_s^+ \to Xe^+\nu_e)/\Gamma(D^0 \to Xe^+\nu_e) = 0.828 \pm 0.051 \pm 0.025$. The ratio of D^+ and D^0 is consistent with the isospin symmetry prediction of unity, and the ratio of D_s^+ and D^0 differs from unity, as expected.

DOI: 10.1103/PhysRevD.81.052007 PACS numbers: 13.20.Fc

I. INTRODUCTION

As part of the CLEO-c analyses of exclusive [1–7] and inclusive semileptonic decays [8], this article presents measurements of D^0, D^+, and D_s^+ inclusive semileptonic branching fractions using the complete CLEO-c data sets. Using these results and known lifetimes, we also report the ratios of the widths $\Gamma(D^+ \to Xe^+\nu_e)/\Gamma(D^0 \to Xe^+\nu_e)$ (which is expected to be unity due to isospin symmetry) and $\Gamma(D_s^+ \to Xe^+\nu_e)/\Gamma(D^0 \to Xe^+\nu_e)$ (which is not expected to be unity [9,10], though with poor theoretical precision). These measurements are important in their own right, and, due to similarities between the D and B sectors, will also improve understanding of B semileptonic decays. In particular, knowledge of the previously unmeasured ratio $\Gamma(D_s^+ \to Xe^+\nu_e)/\Gamma(D^0 \to Xe^+\nu_e)$ enables a more reliable prediction of the difference of the inclusive decay rates between B^0 and B^+ mesons in $b \to u\ell^+\nu_\ell$ decays, thereby reducing theoretical uncertainty [9] in determination of weak mixing parameter V_{ub}.

Two sets of open-charm data samples are used to study the semileptonic decays of charm and charmed-strange mesons. In e^+e^- collisions provided by the Cornell Electron Storage Ring (CESR), the CLEO-c detector has collected integrated luminosities of 818 pb^{-1} at the center-of-mass energy $E_{\rm CM} = 3.774$ GeV near the peak of the $\psi(3770)$ resonance which decays to $D\bar{D}$ pairs, and 602 pb^{-1} at $E_{\rm CM} = 4.170$ GeV near the peak production of $D_s^{*\pm}D_s^{\mp}$ pairs. The former data set contains 3.0×10^6 $D^0\bar{D}^0$ and 2.4×10^6 D^+D^- pairs, and is used to study D^0 and D^+ semileptonic decays. The latter data set contains 0.6×10^6 $D_s^{*\pm}D_s^{\mp}$ pairs, and is used to study D_s^+ semileptonic decays. We have previously reported [8] measurements of inclusive semileptonic decay branching fractions of D^0 and D^+ mesons with a subsample of the former data set.

The remainder of this article is organized as follows. The CLEO-c detector is described in Sec. II. Event reconstruction and selection criteria are described in Sec. III. The analysis procedure to extract semileptonic decay rates is covered in Sec. IV. Results for inclusive spectra are presented in Sec. V. Systematic uncertainty in our measurements is evaluated in Sec. VI. Finally, in Sec. VII a summary of our results is provided.

II. THE CLEO-C DETECTOR

The CLEO-c detector [11–14] is a general-purpose solenoidal detector equipped with four concentric components: a six-layer vertex drift chamber, a 47-layer main drift chamber, a ring-imaging Cherenkov (RICH) detector, and a cesium iodide electromagnetic calorimeter. The detector provides acceptance of 93% of the full 4π solid angle for both charged particles and photons. The main drift chamber provides specific-ionization (dE/dx) measurements that discriminate between charged pions and kaons. The RICH detector covers approximately 80% of 4π and provides additional separation of pions and kaons at high momentum ($\geq$ 700 MeV). Electron identification is based on a likelihood variable that combines the information from the RICH detector, dE/dx, and the ratio of electromagnetic shower energy to track momentum (E/p). A GEANT-based [15] Monte Carlo (MC) simulation is used to study efficiencies of signal and background events. Physics events are generated by EVTGEN [16], tuned with improved knowledge of charm decays [17–20], and final-state radiation (FSR) is modeled by PHOTOS [21].

III. EVENT SELECTION

Charm or charmed-strange mesons are always produced in pairs in our open-charm data samples. Since the data are taken just above threshold, the mesons are produced in a very clean environment with no additional particles except, in the case of the $D_sD_s^*$, a photon or a neutral pion from the D_s^* decay. The analysis proceeds by first defining a single tag (ST) sample, in which one of the D (or D_s) mesons in a $D\bar{D}$ (or $D_sD_s^*$) event is reconstructed in a chosen hadronic decay mode, and a further double tag (DT) subsample in which an additional recoiling electron (or positron) is required as a signature of the signal semileptonic decay. Absolute semileptonic branching fractions for charm or charmed-strange mesons can then be obtained from the fraction of the ST sample that is DT, without requiring any knowledge of the integrated luminosity or how many mesons are produced.

A. Tag selection

To minimize the combinatorial backgrounds and systematic uncertainties, three very clean tag modes composed of only charged particles are used: $\bar{D}^0 \to K^+\pi^-$, $D^- \to K^+\pi^-\pi^-$, and $D_s^- \to \phi\pi^-$. Here, the notation $D_s^- \to \phi\pi^-$ is a shorthand label for $D_s^- \to K^-K^+\pi^-$ events within a 10 MeV mass window of the ϕ meson peak in K^-K^+ invariant mass. The inclusion of charge conjugate modes is implied throughout this article unless otherwise stated.

We identify a ST in the $\psi(3770)$ data sample using the energy difference $\Delta E = E_D - E_{\rm beam}$ and the beam-constrained mass difference $\Delta M_{\rm bc} = [E_{\rm beam}^2 - \mathbf{p}_D^2]^{1/2} - m_D$, where E_D is the energy of the tag, $E_{\rm beam}$ is the beam energy, $\mathbf{p}_D$ is the three momentum of the tag, and m_D is the nominal mass [17] of the neutral or charged charm meson. We require the $\bar{D}^0 \to K^+\pi^-$ and $D^- \to K^+\pi^-\pi^-$ tags to have $\Delta M_{\rm bc}$ within a 4 MeV mass window around the nominal D mass.

For data collected at the center-of-mass energy of 4170 MeV, we identify a ST by using the invariant mass of the tag $M(D_s)$ and recoil mass against the tag $M_{\rm recoil}(D_s)$. The recoil mass is defined as $M_{\rm recoil}(D_s) = [(E_{ee} - E_{D_s})^2 - (\mathbf{p}_{ee} - \mathbf{p}_{D_s})^2]^{1/2}$, where $(E_{ee}, \mathbf{p}_{ee})$ is the

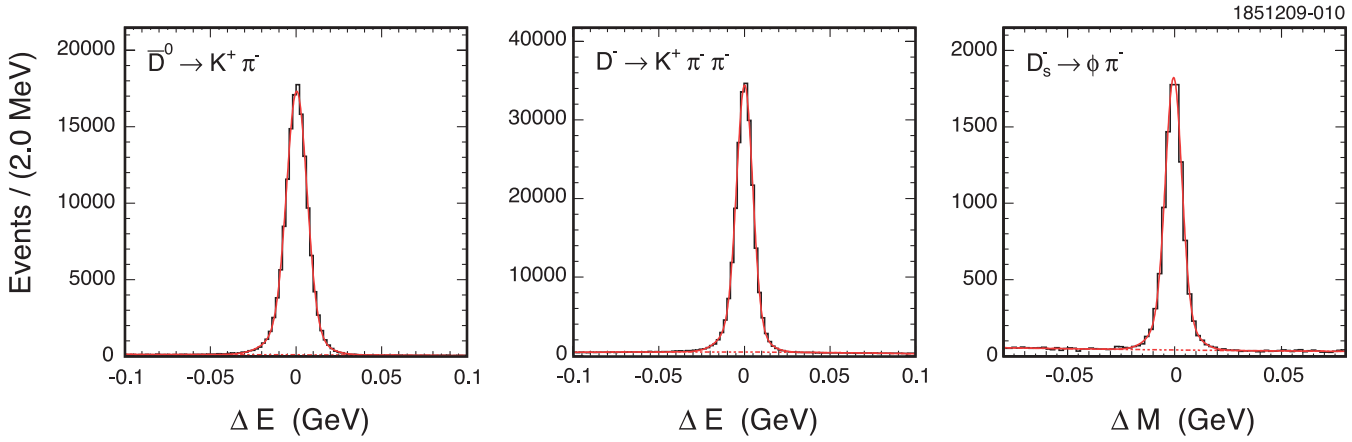

FIG. 1 (color online). Tag ΔE and ΔM distributions in data (histograms) with fits (solid curves) and background contributions (dashed lines).

net four-momentum of the e^+e^- beam taking the finite beam crossing angle into account, and $(E_{D_s}, \mathbf{p}_{D_s})$ is the four-momentum of the tag, with E_{D_s} computed from $\mathbf{p}_{D_s}$ and the nominal mass [17] of the D_s meson. We require the recoil mass to be within 55 MeV of the D_s^* mass [17]. This loose window allows both primary and secondary (from $D_s^{*-} \to D_s^- \gamma$ or $D_s^{*-} \to D_s^- \pi^0$) D_s tags to be selected. We veto tag candidates with track momenta below 100 MeV to reduce the background from $D\bar{D}^*$ decays (through $D^* \to \pi D$).

The ΔE and ΔM distributions obtained from data are shown in Fig. 1. To estimate the backgrounds from the wrong tag combinations, we use the sidebands of the ΔE distribution or the tag mass difference $\Delta M = M(D_s) - m_{D_s}$ distribution, where m_{D_s} is the nominal mass [17] of the D_s meson. We define the signal and sideband regions in Table I. We fit the distributions to a sum of a double-Gaussian function (for signal) and a second order Chebyshev polynomial function (for background) to determine the tag sideband scaling factor $s_{\rm tag}$, which is the ratio of areas in the signal and sideband regions described by the background polynomial function. Obtained ST yields and tag sideband scaling factors are listed in Table II.

TABLE I. Signal and sideband regions of ΔE and ΔM for each tag mode.

Tag mode	Signal (MeV)	Sideband (MeV)
$\bar{D}^0 \to K^+\pi^-$	$-30 \le \Delta E < +30$	$-80 \le \Delta E < -50$
		$+50 \le \Delta E < +80$
$D^- \to K^+\pi^-\pi^-$	$-25 \le \Delta E < +25$	$-65 \le \Delta E < -40$
		$+40 \le \Delta E < +65$
$D_s^- \to \phi\pi^-$	$-20 \le \Delta M < +20$	$-55 \le \Delta M < -35$
		$+35 \le \Delta M < +55$

TABLE II. ST yields and statistical uncertainties in data, where $n_{\rm ST}^S$ is the yield in the tag signal region, $n_{\rm ST}^B$ is the yield in the tag sideband region, $s_{\rm tag}$ is the tag sideband scaling factor obtained from a fit to tag ΔE (or ΔM) distribution, and $n_{\rm ST}$ is the scaled sideband subtracted ST yield.

Tag mode	$n_{\rm ST}^S$	$n_{\rm ST}^B$	$s_{\rm tag}$	$n_{\rm ST}$
$\bar{D}^0 \to K^+\pi^-$	144 260	2258	1.067	141 851 ± 383
$D^- \to K^+\pi^-\pi^-$	231 429	7748	1.104	222 872 ± 490
$D_s^- \to \phi\pi^-$	10 453	807	0.979	9663 ± 106

B. Signal selection

We form DT candidates from ST candidates by adding a recoiling charged track that is consistent with coming from the nominal interaction point. Specifically, the recoiling track's point of closest approach to the origin must be within 5 cm of the interaction point along the beam line and within 5 mm of the interaction point in the plane transverse to the beam line. We require the momentum of the track to be $p \ge 200$ MeV and the angle with respect to the beam to be $|\cos\theta| < 0.80$ so that all charged-particle identification (PID) information (dE/dx, RICH, and E/p) is available. The signal track in the DT candidate is also required to be identified as an electron, a charged pion, or a charged kaon, for further analysis. This is discussed in the next section.

IV. ANALYSIS

The D (or D_s) semileptonic inclusive spectrum (or differential decay rate) can be expressed as

$$\frac{d\mathcal{B}_{\rm SL}}{dp} = \frac{1}{n_D}\frac{\Delta n_e}{\Delta p} = \frac{1}{n_{\rm ST}}\frac{\Delta n_{\rm DT}/\epsilon_{\rm SL}}{\Delta p}, \quad (1)$$

where n_D is the number of D mesons produced, n_e is the number of produced primary electrons in bins of momentum p, $n_{\rm ST}$ is the number of ST, $\Delta n_{\rm DT}$ is the electron candidate yield in bins of momentum, and $\epsilon_{\rm SL}$ is the (momentum-dependent) electron detection efficiency.

The D semileptonic branching fraction can be obtained by integrating the differential spectrum and correcting for the 200 MeV momentum cutoff by extrapolating the spectrum below the cutoff. If we had a perfect MC modeling of the semileptonic decays, a simple momentum bin-by-bin correction factor could be used for $\epsilon_{\rm SL}$. Instead, we use a more general unfolding [22] approach to minimize MC model dependence.

The observed laboratory momentum spectrum $y(b, i_{\rm track})$ of a particle identified as type b ($= e$, π, or K) in bins of measured track momentum bin $i_{\rm track}$ can be modeled as a folded distribution. It is related to the true laboratory momentum $n(a, j)$ via detector-response matrices that account for resolution and efficiency:

$$y(b, i_{\rm track}) = \sum_a A_{\rm PID}(b|a, i_{\rm track}) \sum_j A_{\rm track}(i_{\rm track}|a, j) n(a, j), \tag{2}$$

where a ($= e$, μ, π, or K) is the true particle species index, $n(a, j)$ is the true laboratory momentum spectrum in bins of true laboratory momentum bin index j of a particle type a, $A_{\rm track}(i_{\rm track}|a, j)$ is the tracking efficiency matrix, which describes the probability of a particle of type a with momentum in bin j to be reconstructed in track momentum bin $i_{\rm track}$, and $A_{\rm PID}(b|a, i_{\rm track})$ is the PID efficiency matrix, which describes the probability of a particle of type a with measured momentum in bin $i_{\rm track}$ to be identified as PID type b. We unfold [22] Eq. (2) to obtain the true momentum spectrum

$$n(a = e, j) = \sum_{i_{\rm track}} A^{-1}_{\rm track}(i_{\rm track}|a = e, j) \times \left[\sum_b A^{-1}_{\rm PID}(b|a, i_{\rm track}) y(b, i_{\rm track}) \right]_{a=e}, \tag{3}$$

where the A^{-1}'s are the unfolded inverses of each efficiency matrix. Because we are interested in the primary electron laboratory momentum spectrum (to obtain the branching fraction) we use the electron solution after PID unfolding ($a = e$).

In addition to finite resolution and efficiency, modeled by detector-response matrices, we have to consider possible backgrounds in our observed spectrum. We remove combinatorial wrong-tag background contribution by ΔE (or ΔM) sideband subtraction. Charge symmetric nonprimary true electron backgrounds (from γ conversion and π^0 Dalitz decay) are subtracted by using the wrong-sign (WS, opposite to the expected primary electron charge) electron sample. In the following subsections, we break the analysis described above into discrete steps.

A. PID yield

From a set of signal candidate tracks, we measure the PID yield $y(b, i)$ in bins of PID type b, track momentum bin $i_{\rm track}$, ΔE (or ΔM) signal and sideband regions $i_{\rm SB}$, and right-sign (RS) or wrong-sign (WS) bin $i_{\rm RW}$ depending on the charge of the track and the flavor of the tag, where i is a collective index for $(i_{\rm track}, i_{\rm SB}, i_{\rm RW})$. The charge of the daughter kaon defines the flavor of the $\bar{D}^0 \to K^+\pi^-$ tag, and the charge of the tag defines $D^- \to K^+\pi^-\pi^-$ and $D_s^- \to \phi\pi^-$ tags. The RS track is defined to be the track with the same charge as the tagged $\bar{D}^0$ daughter kaon or to be the opposite charge of the charged tags, and the WS track is defined the other way around.

B. PID unfolding

We correct for PID efficiency and mis-PID crossfeed backgrounds using

$$y(a, i) = A^{-1}_{\rm PID}(b|a, i) y(b, i), \tag{4}$$

where i is a collective index for $(i_{\rm track}, i_{\rm SB}, i_{\rm RW})$. The PID matrix $A_{\rm PID}(b|a)$ used in the unfolding is shown in Fig. 2. PID matrix elements associated with the charged pion are obtained from $K^0_S \to \pi^+\pi^-$ events, the charged kaon elements are obtained from $D^+ \to K^-\pi^+\pi^+$ events, and the electron elements are obtained from radiative Bhabha events ($e^+e^-\gamma$) embedded in hadronic events. Here we treat muons as pions because muons in the momentum range in which we are interested behave almost the same as charged pions in the CLEO-c detector. The effect of this approximation is negligible on our branching fraction measurement because the probability of pions (and muons) to be misidentified as electrons is very small, as shown in Fig. 2. After solving the PID problem, we take the electron solution ($a = e$) for further analysis.

C. Tag sideband subtraction

To remove the wrong-tag combinatorial background, we perform ΔE (or ΔM) sideband subtractions after PID unfolding. After this process, we deal with real electrons from D (or D_s) meson decay.

D. Wrong-sign electron subtraction

Charge symmetric secondary electrons are removed by subtracting the WS (secondary) electron yield from the RS (primary plus secondary) electron yield. After this process, we end up with primary electrons from D (or D_s) meson decay.

E. Tracking efficiency, $A_{\rm track}$

We obtain the tracking efficiency matrix $A_{\rm track}(i_{\rm track}|j)$ from MC simulation. This includes track finding efficiency and resolution effects.

F. Tag bias correction

The signal semileptonic efficiency $\epsilon_{\rm SL}$ requires a possible tag bias correction which would be introduced if the ST efficiency in the signal DT events is different from that when the other recoiling system is a generic D-meson (or

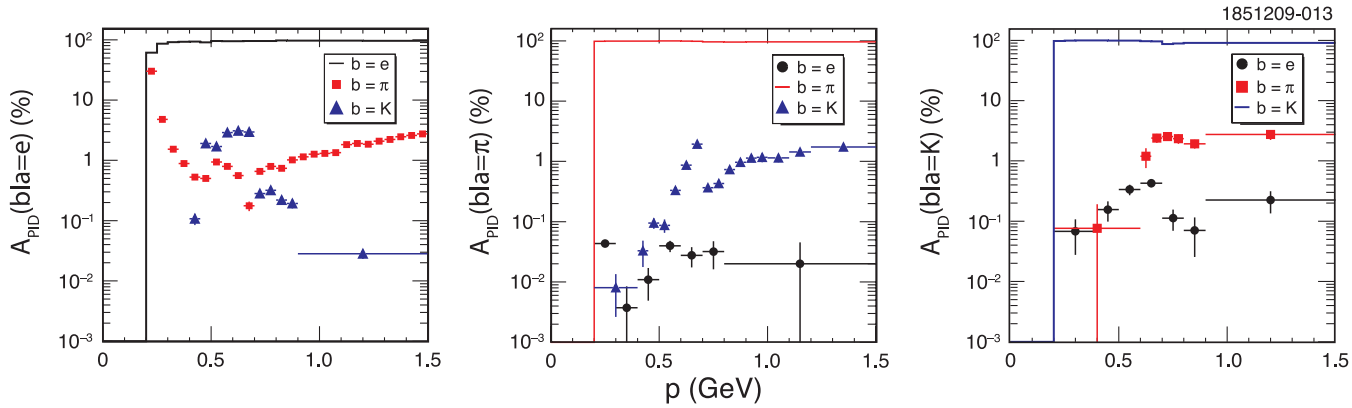

FIG. 2 (color online). The components of the PID efficiency matrix $A_{\rm PID}(b|a)$ obtained from data. The matrix describes the probability of a particle of type a to be identified as a PID type b. We measured the PID matrix in momentum intervals of 50 MeV (some bins are wider due to low statistics) above the PID momentum cutoff 200 MeV. The cases with $a \neq b$, conventionally called the fake rate or mis-PID probability, are shown in points with statistical uncertainties. The cases with $a = b$, conventionally called the efficiency, are shown as solid lines. The discontinuities at momentum 700 MeV in fake rates and efficiencies are due to the fact that the RICH information is used for pion and kaon identifications only above 700 MeV.

D_s-meson) decay. The effect of the tag bias can be express in terms of a ST efficiency ratio

$$\epsilon_{\rm SL} = \frac{\epsilon_{\rm DT}}{\epsilon_{\rm ST}} = \frac{\epsilon_{\rm DT}}{\epsilon'_{\rm ST}}\frac{\epsilon'_{\rm ST}}{\epsilon_{\rm ST}} = \frac{\epsilon_e \epsilon'_{\rm ST}}{\epsilon'_{\rm ST}}\frac{\epsilon'_{\rm ST}}{\epsilon_{\rm ST}} = \epsilon_e b_{\rm tag}, \quad (5)$$

where $\epsilon_{\rm DT}$ is the DT efficiency, $\epsilon_{\rm ST}$ is the ST efficiency against generic decays in the recoiling system, $\epsilon'_{\rm ST}$ is the ST efficiency when the recoiling system is the signal semileptonic decays, ϵ_e is the signal electron detection efficiency given the tag in the other side is found, and $b_{\rm tag}$ is a measure of tag bias in the efficiency Thus, $b_{\rm tag} = \epsilon'_{\rm ST}/\epsilon_{\rm ST}$ and $\epsilon_e = \epsilon_{\rm DT}/\epsilon'_{\rm ST}$. We expect this effect to be small due to chosen clean tag modes and low event multiplicity. We estimate tag biases in MC simulation: $b_{\rm tag}(D^0 \to e^+X) = 0.9965 \pm 0.0017$, $b_{\rm tag}(D^+ \to e^+X) = 1.0017 \pm 0.0021$, and $b_{\rm tag}(D_s^+ \to e^+X) = 1.0069 \pm 0.0021$, where uncertainties are due to MC statistics.

G. Doubly Cabibbo-suppressed decay correction

Because of the doubly Cabibbo-suppressed decay (DCSD) and quantum correlation [23,24] in coherent $D^0\bar{D}^0$ production at the $\psi(3770)$ resonance energy, we need a correction for the observed semileptonic branching fraction using the $\bar{D}^0 \to K^-\pi^+$ tag mode. The observed branching fraction $\mathcal{B}_{\rm obs}$ requires a correction [23,24]

$$\mathcal{B}(D^0 \to Xe^+\nu_e) = \frac{1 + R_{\rm WS}}{1 - r^2}\mathcal{B}_{\rm obs}(D^0 \to Xe^+\nu_e). \quad (6)$$

Here $r^2 = |\langle K^+\pi^-|D^0\rangle/\langle K^+\pi^-|\bar{D}^0\rangle|^2$ is the ratio of the DCSD rate to the Cabibbo-favored decay rate, and $R_{\rm WS} = \Gamma(D^0 \to K^+\pi^-)/\Gamma(\bar{D}^0 \to K^+\pi^-)$ is the ratio of the time-integrated DCSD rate to the Cabibbo-favored decay rate. Using the world average [17] values of these we need a correction factor $(1 + R_{\rm WS})/(1 - r^2) = [1 + (3.80 \pm 0.05) \times 10^{-3}]/[1 - (3.35 \pm 0.09) \times 10^{-3}] = 1.0072 \pm 0.0001$.

V. RESULTS

The final electron candidate yields are summarized in Table III and efficiency-corrected laboratory momentum spectra are shown in Fig. 3. Also shown in Fig. 3 are the spectrum extrapolations below the PID momentum cutoff (200 MeV). The curves shown are obtained with a fit using the sum of measurements of exclusive channels together with form-factor models and adding higher-resonance and nonresonant channels to match the sum of the exclusive channels with our measured branching fraction. Further details of the extrapolation procedure are available in the Appendix. From the fit results, we obtain fractions below the momentum cutoff of 7.8% for D^0, 8.0% for D^+, and 7.0% for D_s^+.

At this point, we also consider the secondary electrons from leptonic decays of $D^+ \to \tau^+\nu_\tau$ and $D_s^+ \to \tau^+\nu_\tau$ as they produce electrons through $\tau^+ \to e^+\nu_e\bar{\nu}_\tau$ decay. This source of secondary electrons is expected to be large in D_s^+, so we have included the expected spectrum component in the extrapolation. The expected branching fractions of these secondary electrons from the leptonic decays of D^+ and D_s^+ are subtracted from the fully inclusive branching fraction results to obtain inclusive semileptonic decay branching fractions. The branching fraction for $D_s^+ \to \tau^+\nu_\tau$ decay is taken from Refs. [25,26], $\mathcal{B}(D_s^+ \to \tau^+\nu_\tau) = (5.62 \pm 0.41 \pm 0.16)\%$. The size of the expected secondary electron contribution from the unobserved leptonic decay $D^+ \to \tau^+\nu_\tau$ is based on the known branching fraction of $D^+ \to \mu^+\nu_\mu$ decay [27] scaled by the standard model decay rate ratio [17] $\Gamma(D^+ \to \tau^+\nu_\tau)/\Gamma(D^+ \to \mu^+\nu_\mu) = 2.67$. We take the uncertainty in the $\tau \to e$

TABLE III. Summary of DT yields, statistical uncertainties, and correction procedure explained in Sec. IV. PID yields (Sec. IV A) for electron candidates ($b = e$) are shown in the first group for tag signal region (S), tag sideband region (B), right-sign (R), and wrong-sign (W) bins, where the yields in the sideband region are scaled by the tag sideband scaling factor (Table II) for each tag mode. PID unfolded (Sec. IV B) electron yields ($a = e$) are shown in the second group. Tag sideband subtracted (Sec. IV C) electron yields are shown in the third group, followed by the wrong-sign subtracted yield (Sec. IV D), tracking efficiency-corrected yield (Sec. IV E), and remaining tag bias (Sec. IV F) or DCSD (Sec. IV G) corrected yield.

	D^0	D^+	D_s^+
PID yield, electron candidates			
$y(b = e, S, R)$	6618.0 ± 81.4	24 834.0 ± 157.6	553.0 ± 23.5
$y(b = e, B, R)$	41.6 ± 6.7	332.4 ± 19.2	24.5 ± 4.9
$y(b = e, S, W)$	653.0 ± 25.6	711.0 ± 26.7	50.0 ± 7.1
$y(b = e, B, W)$	19.2 ± 4.5	55.2 ± 7.8	9.8 ± 3.1
PID unfolded yield, electrons			
$y(a = e, S, R)$	7292.4 ± 90.7	27 304.5 ± 174.8	608.9 ± 26.4
$y(a = e, B, R)$	47.1 ± 7.7	370.4 ± 21.7	27.7 ± 5.6
$y(a = e, S, W)$	682.4 ± 31.4	812.8 ± 33.8	56.7 ± 8.6
$y(a = e, B, W)$	21.3 ± 5.3	65.2 ± 9.8	11.7 ± 3.4
Tag sideband subtracted electrons			
$y(a = e, R)$	7245.3 ± 91.0	26 934.1 ± 176.2	581.2 ± 27.0
$y(a = e, W)$	661.1 ± 31.9	747.6 ± 35.2	44.9 ± 9.2
Wrong-sign subtracted electrons	6584.2 ± 96.4	26 186.5 ± 179.6	536.3 ± 28.5
Tracking efficiency-corrected electrons	8361.0 ± 123.0	33 182.0 ± 228.2	681.3 ± 36.4
Tag bias (and DCSD) corrected electrons	8450.8 ± 124.3	33 125.6 ± 227.9	676.6 ± 36.2

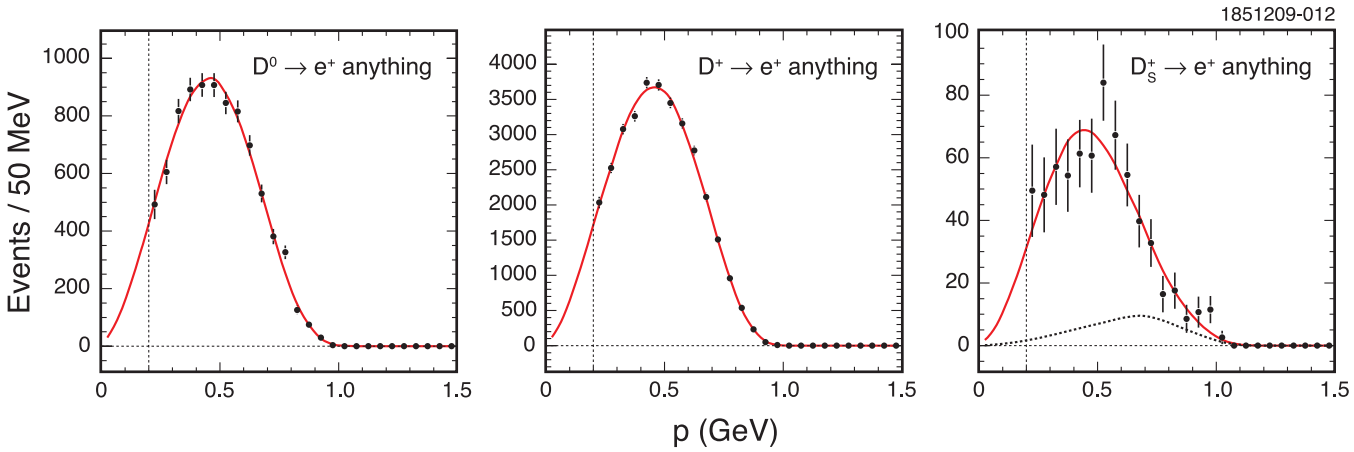

FIG. 3 (color online). Inclusive laboratory frame electron spectra obtained from data, shown as points with statistical uncertainties. The vertical dashed lines indicate the PID momentum cutoff at 200 MeV. Extrapolated spectra are shown as solid curves. The dashed curve in the D_s^+ spectrum plot is the expected contribution from $\tau^+ \to e^+ \nu_e \bar{\nu}_\tau$ from leptonic $D_s^+ \to \tau^+ \nu_\tau$ decay.

TABLE IV. Summary of semileptonic branching fractions. Here $\mathcal{B}_{\text{trunc}}$ is the partial branching fraction above 200 MeV, $\mathcal{B}(e^+X)$ is the extrapolated full branching fraction, and $\mathcal{B}(Xe^+\nu_e)$ is the semileptonic branching fraction after $\tau \to e$ correction (for D^+ and D_s^+). First uncertainties are statistical and the second are systematic due to uncertainties in $\mathcal{B}(D^+ \to \tau^+ \nu_\mu)$ [27], $\mathcal{B}(D_s^+ \to \tau^+ \nu_\tau)$ [25,26], and $\mathcal{B}(\tau^+ \to e^+ \nu_e \bar{\nu}_\tau)$ [17].

Tag mode	$B_{\text{trunc}}(e^+X)$ (%)	$B(e^+X)$ (%)	$B(Xe^+\nu_e)$ (%)
$\bar{D}^0 \to K^+\pi^-$	5.958 ± 0.084	6.460 ± 0.091	6.460 ± 0.091
$D^- \to K^+\pi^-\pi^-$	14.863 ± 0.092	16.147 ± 0.100	16.129 ± 0.100 ± 0.000
$D_s^- \to \phi\pi^-$	7.002 ± 0.361	7.525 ± 0.387	6.522 ± 0.387 ± 0.079

TABLE V. Inclusive semileptonic electron partial branching fractions of D^0, D^+, and D_s^+ in the laboratory frame. For D^+ and D_s^+, we have subtracted expected contributions from leptonic decays $\tau^+\nu_\tau$ (followed by $\tau^+ \to e^+\nu_e\bar{\nu}_\tau$). Systematic uncertainties in total branching fractions are added to the statistical uncertainties. In comparing theoretical predictions with these measurements, one must smear the theoretical predictions by boosting from the D (or D_s) rest frame to the laboratory frame. For D_s, 51% of the electrons are from secondary D_s from D_s^*, and 49% are from primary D_s.

p (GeV)	$\Delta B(D^0 \to Xe^+\nu_e)$ (%)	$\Delta B(D^+ \to Xe^+\nu_e)$ (%)	$\Delta B(D_s^+ \to Xe^+\nu_e)$ (%)
0.200–0.250	0.347 ± 0.036	0.912 ± 0.040	0.491 ± 0.152
0.250–0.300	0.426 ± 0.030	1.133 ± 0.038	0.470 ± 0.124
0.300–0.350	0.576 ± 0.031	1.379 ± 0.041	0.554 ± 0.126
0.350–0.400	0.629 ± 0.030	1.462 ± 0.043	0.515 ± 0.120
0.400–0.450	0.640 ± 0.031	1.675 ± 0.047	0.578 ± 0.112
0.450–0.500	0.640 ± 0.031	1.661 ± 0.046	0.562 ± 0.123
0.500–0.550	0.596 ± 0.029	1.546 ± 0.044	0.794 ± 0.127
0.550–0.600	0.575 ± 0.029	1.415 ± 0.041	0.611 ± 0.115
0.600–0.650	0.492 ± 0.026	1.243 ± 0.038	0.471 ± 0.104
0.650–0.700	0.374 ± 0.023	0.946 ± 0.032	0.314 ± 0.087
0.700–0.750	0.269 ± 0.019	0.674 ± 0.026	0.246 ± 0.079
0.750–0.800	0.230 ± 0.017	0.429 ± 0.019	0.089 ± 0.060
0.800–0.850	0.089 ± 0.011	0.240 ± 0.014	0.115 ± 0.060
0.850–0.900	0.053 ± 0.008	0.103 ± 0.009	0.037 ± 0.046
0.900–0.950	0.021 ± 0.005	0.022 ± 0.004	0.074 ± 0.051
0.950–1.000	0.002 ± 0.002	0.004 ± 0.002	0.096 ± 0.045
1.000–1.050	...	...	0.015 ± 0.022

correction as a part of our systematic uncertainty. Branching fraction results are summarized in Table IV with all above-mentioned efficiency and cutoff corrections.

The laboratory frame electron momentum spectra shown in Fig. 3 are given in tabular form in Table V.

VI. SYSTEMATIC UNCERTAINTIES

Possible sources of systematic uncertainties and their effects on the branching fraction measurements are summarized in Table VI.

The ST yields are obtained from a tag (ΔE or ΔM) sideband subtraction method. Because of the chosen clean tag modes, there is very little combinatorial background under the signal peak, as shown in Fig. 1. Systematic uncertainties in the numbers of tags are studied by using alternative signal and background functions, and comparing the known input number of ST in a MC simulation test to the output with the same procedure. By adding all of the resulting variations in quadrature, we obtain 0.5% (in D^0), 0.7% (in D^+), and 0.9% (in D_s^+) uncertainties in the estimation of the number of ST.

TABLE VI. Summary of sources of systematic uncertainty and their effects on the semileptonic branching fraction measurements.

Source	D^0 (%)	D^+ (%)	D_s^+ (%)
Number of tags	0.5	0.7	0.9
Tracking	0.3	0.3	0.3
PID	0.8	0.5	0.6
FSR	0.5	0.5	0.5
Tag bias	0.2	0.2	0.3
DCSD	0.0	...	...
$\tau \to e$	...	0.0	1.2
Extrapolation	1.3	1.4	1.5
Total	1.7	1.8	2.3

The systematic uncertainty of 0.3% in tracking efficiency was estimated [18] in a detailed MC and data efficiency comparison using $\psi(3770) \to D\bar{D}$ events with the cases when both D and $\bar{D}$ mesons can be fully reconstructed.

Uncertainties in FSR and bremsstrahlung effects on D semileptonic decay branching fraction measurements were studied in our previous measurement [8] and in high statistics exclusive D semileptonic decay modes [5]. They are found to be well simulated in our MC program. We have assessed the uncertainty in FSR by redoing the analysis using alternative signal efficiency and input spectra with FSR turned off in the MC simulation. Including the uncertainty in bremsstrahlung simulation [5], we assign 0.5% uncertainty due to FSR and bremsstrahlung effects on our branching fraction measurements.

Uncertainties in electron identification for semileptonic decays are assessed by comparing the efficiency measured using a radiative Bhabha sample embedded in hadronic events to those in various MC simulated event samples. We assign systematic uncertainties due to electron identifica-

tion as 0.7% for $D^0 \to Xe^+\nu_e$, 0.5% for $D^+ \to Xe^+\nu_e$, and 0.6% for $D_s^+ \to Xe^+\nu_e$. For other PID efficiencies, we have varied their values within measured uncertainties and observe the effect on our measured branching fraction. By adding all electron identification and other PID uncertainties in quadrature we assign uncertainties in PID as 0.8% for $D^0 \to Xe^+\nu_e$, 0.5% for $D^+ \to Xe^+\nu_e$, and 0.6% for $D_s^+ \to Xe^+\nu_e$.

Tag bias corrections are estimated from MC simulation. We take the uncertainty in the MC statistics and a quarter of the size of the tag bias as the uncertainty in the correction.

For the D_s^+ and D^+ inclusive electron spectra, we subtract the contribution from $\tau^+ \to e^+\nu_e\bar{\nu}_\tau$ as estimated in Table VIII (and Table IX) to obtain the inclusive semileptonic branching fraction. We take the uncertainty from $\mathcal{B}(D_s^+ \to \tau^+\nu_\tau)$ [and $\mathcal{B}(D^+ \to \tau^+\nu_\tau)$] listed in the table for the uncertainty on the $\tau \to e$ contribution correction. The uncertainty in $D^+ \to Xe^+\nu_e$ is negligible, and we assign an uncertainty of 1.2% in $D_s^+ \to Xe^+\nu_e$.

To estimate systematic uncertainties in the extrapolation procedure, we fix all parameters to the reference values listed in Tables VII, VIII, and IX. Then we vary each semileptonic decay component one-by-one within the allowed range of uncertainties, listed in the table, and reevaluate the fraction below the momentum cutoff and the effect on the resulting branching fraction. For the unobserved decay components, we vary 100% of the size of the predicted branching fraction to assess the uncertainty. We also use alternative form-factor models, by changing models component-by-component from the reference models in the tables, when we perform an extrapolation fit as described in the Appendix, to assess the additional uncertainty in the extrapolation. By adding all effects in quadrature, we assign 1.3% for $D^0 \to Xe^+\nu_e$, 1.4% for $D^+ \to Xe^+\nu_e$, and 1.5% for $D_s^+ \to Xe^+\nu_e$ as uncertainties in the extrapolation procedure.

VII. SUMMARY

Using the full sample of open-charm data collected by the CLEO-c detector, we obtain the charm and charmed-strange meson inclusive semileptonic branching fractions:

$$\mathcal{B}(D^0 \to Xe^+\nu_e) = (6.46 \pm 0.09 \pm 0.11)\%,$$

$$\mathcal{B}(D^+ \to Xe^+\nu_e) = (16.13 \pm 0.10 \pm 0.29)\%,$$

and

$$\mathcal{B}(D_s^+ \to Xe^+\nu_e) = (6.52 \pm 0.39 \pm 0.15)\%,$$

where the first uncertainties are statistical and the second are systematic. Using known [17] lifetimes $\tau_{D^0} = (410.1 \pm 1.5) \times 10^{-15}$ s, $\tau_{D^+} = (1040 \pm 7) \times 10^{-15}$ s, and $\tau_{D_s^+} = (500 \pm 7) \times 10^{-15}$ s, we obtain the ratios of semileptonic decay widths

$$\frac{\Gamma(D^+ \to Xe^+\nu_e)}{\Gamma(D^0 \to Xe^+\nu_e)} = 0.985 \pm 0.015 \pm 0.024$$

and

$$\frac{\Gamma(D_s^+ \to Xe^+\nu_e)}{\Gamma(D^0 \to Xe^+\nu_e)} = 0.828 \pm 0.051 \pm 0.025.$$

In these ratios, we assume the PID and tracking uncertainties are fully correlated and all others are uncorrelated. The former ratio shows that charged and neutral charm meson semileptonic decay widths are consistent with isospin symmetry, as expected, because the two mesons differ only in the isospin of the light quark. On the other hand, the latter ratio shows that there is an indication of difference between charm and charmed-strange meson semileptonic decay widths.

ACKNOWLEDGMENTS

We gratefully acknowledge the effort of the CESR staff in providing us with excellent luminosity and running conditions. D. Cronin-Hennessy thanks the A. P. Sloan Foundation. This work was supported by the National Science Foundation, the U.S. Department of Energy, the Natural Sciences and Engineering Research Council of Canada, and the U.K. Science and Technology Facilities Council.

APPENDIX: SPECTRUM EXTRAPOLATION

Charm and charmed-strange exclusive semileptonic decay components used to perform spectrum extrapolation fits are summarized in Tables VII, VIII, and IX. Efficiency-corrected data points are fit to a sum of exclusive semileptonic decay components to estimate the unmeasured portion of the spectrum below the momentum cutoff at 200 MeV due to the electron identification. Normalization of each component is allowed to float within the uncertainty shown in the tables.

Higher-resonance and nonresonant decay components are used to make the sum of exclusive branching fractions match the inclusive branching fraction in D^0 and D^+ extrapolations. Higher-resonance decay branching fractions are predicted by the ISGW2 [10] form-factor model and remaining gaps are filled by nonresonant decays. We assume the size of the nonresonant component of $D \to \bar{K}\pi e^+\nu_e$ to be about 5% [17,29]. Uncertainties of unobserved higher-resonance channels are assumed to be $\pm 100\%$ of the predicted branching fractions.

The expected leptonic decay contributions due to the $\tau^+ \to e^+\nu_e\bar{\nu}_\tau$ decay in D^+ and D_s^+ are used to correct nonsemileptonic electrons in our measurements as shown in Tables VIII and IX. For D_s^+ decays, this component is expected to be large, and we include the leptonic decay component in the extrapolation fit.

TABLE VII. Summary of D^0 semileptonic decays used to perform the spectrum extrapolation. Assumed branching fractions are shown in the second column; normalization of each component is allowed to float within the given uncertainty. Form-factor models used to describe the shape of each spectrum are shown in the third column: single-pole (SPOLE [28]), modified-pole (BK [28]), ISGW2 [10], and phase space (PHSP). Higher-resonance (and nonresonant) channels are used to match the sum of exclusive semileptonic branching fractions to the inclusive semileptonic branching fraction.

Channel	$\mathcal{B}$ (%)	Form factor	Comment
$D^0 \to K^{*-} e^+ \nu_e$	2.16(17) [1]	SPOLE	$r_V = 1.62(8)$ and $r_2 = 0.83(5)$ [17]
$D^0 \to K^- e^+ \nu_e$	3.50(5) [5]	BK	$\alpha_{\rm BK} = 0.30(3)$ [5]
$D^0 \to K_1^- e^+ \nu_e$	0.11(11)	ISGW2	$\mathcal{B}$ from Ref. [10] scaled by Ref. [5]
$D^0 \to K_2^{*-} e^+ \nu_e$	0.11(11)	ISGW2	$\mathcal{B}$ set to same as $D^0 \to K_1^- e^+ \nu_e$
$D^0 \to \bar{K} \pi e^+ \nu_e$	0.12(3) [17,29]	PHSP	Nonresonant
$D^0 \to \pi^- e^+ \nu_e$	0.288(9) [5]	BK	$\alpha_{\rm BK} = 0.21(7)$ [5]
$D^0 \to \rho^- e^+ \nu_e$	0.16(2) [2]	SPOLE	$r_V = 1.4(3)$ and $r_2 = 0.6(2)$ [2]

TABLE VIII. Summary of D^+ semileptonic decays used to perform the spectrum extrapolation. Assumed branching fractions are shown in the second column; normalization of each component is allowed to float within the given uncertainty. Form-factor (FF) models used to describe the shape of each spectrum are shown in the third column: single-pole (SPOLE [28]), modified-pole (BK [28]), ISGW2 [10], and phase space (PHSP). Higher-resonance (and nonresonant) channels are used to match the sum of exclusive semileptonic branching fractions to the inclusive semileptonic branching fraction. The size of the expected secondary electron contribution from the leptonic decay $D^+ \to \tau^+ \nu_\tau$ is shown in the last row based on the known branching fraction of $D^+ \to \mu^+ \nu_\mu$ decay [27] scaled by the standard model decay rate ratio [17] $\Gamma(D^+ \to \tau^+ \nu_\tau)/\Gamma(D^+ \to \mu^+ \nu_\mu) = 2.67$.

Channel	$\mathcal{B}$ (%)	Form factor	Comment
$D^+ \to \bar{K}^{*0} e^+ \nu_e$	5.56(35) [3]	SPOLE	$r_V = 1.62(8)$ and $r_2 = 0.83(5)$ [17]
$D^+ \to \bar{K}^0 e^+ \nu_e$	8.83(22) [5]	BK	$\alpha_{\rm BK} = 0.30(2)$ [17]
$D^+ \to \bar{K}_1^0 e^+ \nu_e$	0.29(29)	ISGW2	$\mathcal{B}$ from Ref. [10] scaled by Ref. [5]
$D^+ \to \bar{K}_2^{*0} e^+ \nu_e$	0.29(29)	ISGW2	$\mathcal{B}$ set to same as $D^+ \to \bar{K}_1^0 e^+ \nu_e$
$D^+ \to \bar{K} \pi e^+ \nu_e$	0.32(8) [17,29]	PHSP	Nonresonant
$D^+ \to \pi^0 e^+ \nu_e$	0.405(18) [5]	BK	$\alpha_{\rm BK} = 0.21(7)$ [5]
$D^+ \to \eta e^+ \nu_e$	0.13(2) [4]	BK	FF set to same as $D^+ \to \pi^0 e^+ \nu_e$ [5]
$D^+ \to \eta' e^+ \nu_e$	0.02(2) [4,10,30]	BK	FF set to same as $D^+ \to \pi^0 e^+ \nu_e$ [5]
$D^+ \to \rho^0 e^+ \nu_e$	0.23(2) [2]	SPOLE	$r_V = 1.4(3)$ and $r_2 = 0.6(2)$ [2]
$D^+ \to \omega e^+ \nu_e$	0.15(3) [2]	SPOLE	FF set to same as $D^+ \to \rho^0 e^+ \nu_e$ [2]
$D^+ \to \tau^+ \nu_\tau$	0.018 [17,27]		

TABLE IX. Summary of D_s^+ leptonic and semileptonic decays used to perform the spectrum extrapolation. Assumed branching fractions are shown in the second column; normalization of each component is allowed to float within the given uncertainty during the fit. Form-factor models used to describe the shape of each spectrum are shown in the third column: single-pole (SPOLE [28]) and ISGW2 [10]. The size of the expected secondary electron contribution from the leptonic decay $D_s^+ \to \tau^+ \nu_\tau$ is shown in the last row based on the known branching fraction of $D_s^+ \to \tau^+ \nu_\tau$ decay [25,26], and the shape is obtained from the EVTGEN [16] MC program.

Channel	$\mathcal{B}$ (%)	Form factor	Comment
$D_s^+ \to \phi e^+ \nu_e$	2.36(26) [7]	SPOLE	$m_V = 2.1$ GeV, $m_A = 2.28$ GeV, $r_V = 1.849(112)$, and $r_2 = 0.763(96)$ from Ref. [31]
$D_s^+ \to \eta e^+ \nu_e$	2.48(32) [6]	ISGW2	
$D_s^+ \to \eta' e^+ \nu_e$	0.91(33) [6]	ISGW2	
$D_s^+ \to K^0 e^+ \nu_e$	0.37(10) [6]	ISGW2	
$D_s^+ \to K^{*0} e^+ \nu_e$	0.18(7) [6]	ISGW2	
$D_s^+ \to f_0 e^+ \nu_e$	0.40(6) [7,32]	SPOLE	$m_{\rm pole} = 1.7$ GeV [7]
$D_s^+ \to \tau^+ \nu_\tau$	1.003(79) [17,25,26]		

[1] T. E. Coan *et al.* (CLEO Collaboration), Phys. Rev. Lett. **95**, 181802 (2005).
[2] Y. Gao, ''Semileptonic Results from CLEO,'' 33rd International Conference on High Energy Physics (ICHEP 06), Moscow, Russia, 2006 (unpublished).
[3] G. S. Huang *et al.* (CLEO Collaboration), Phys. Rev. Lett. **95**, 181801 (2005).
[4] R. E. Mitchell *et al.* (CLEO Collaboration), Phys. Rev. Lett. **102**, 081801 (2009).
[5] D. Besson *et al.* (CLEO Collaboration), Phys. Rev. D **80**, 032005 (2009).
[6] J. Yelton *et al.* (CLEO Collaboration), Phys. Rev. D **80**, 052007 (2009).
[7] K. M. Ecklund *et al.* (CLEO Collaboration), Phys. Rev. D **80**, 052009 (2009).
[8] N. E. Adam *et al.* (CLEO Collaboration), Phys. Rev. Lett. **97**, 251801 (2006).
[9] M. B. Voloshin, Phys. Lett. B **515**, 74 (2001).
[10] D. Scora and N. Isgur, Phys. Rev. D **52**, 2783 (1995).
[11] R. A. Briere *et al.* (CESR-c, CLEO-c Taskforces, and CLEO-c Collaboration), Cornell University LEPP Report No. CLNS 01/1742, 2001 (unpublished).
[12] Y. Kubota *et al.* (CLEO Collaboration), Nucl. Instrum. Methods Phys. Res., Sect. A **320**, 66 (1992).
[13] D. Peterson *et al.*, Nucl. Instrum. Methods Phys. Res., Sect. A **478**, 142 (2002).
[14] M. Artuso *et al.*, Nucl. Instrum. Methods Phys. Res., Sect. A **502**, 91 (2003).
[15] R. Brun *et al.*, GEANT 3.21, CERN Program Library Long Writeup W5013, 1993 (unpublished).
[16] D. J. Lange, Nucl. Instrum. Methods Phys. Res., Sect. A **462**, 152 (2001).
[17] C. Amsler *et al.* (Particle Data Group), Phys. Lett. B **667**, 1 (2008).
[18] S. Dobbs *et al.* (CLEO Collaboration), Phys. Rev. D **76**, 112001 (2007).
[19] J. P. Alexander *et al.* (CLEO Collaboration), Phys. Rev. Lett. **100**, 161804 (2008).
[20] S. Dobbs *et al.* (CLEO Collaboration), Phys. Rev. D **79**, 112008 (2009).
[21] E. Barberio and Z. Wąs, Comput. Phys. Commun. **79**, 291 (1994).
[22] A. Hocker and V. Kartvelishvili, Nucl. Instrum. Methods Phys. Res., Sect. A **372**, 469 (1996).
[23] D. M. Asner and W. M. Sun, Phys. Rev. D **73**, 034024 (2006); **77**, 019901(E) (2008).
[24] J. L. Rosner *et al.* (CLEO Collaboration), Phys. Rev. Lett. **100**, 221801 (2008).
[25] J. P. Alexander *et al.* (CLEO Collaboration), Phys. Rev. D **79**, 052001 (2009).
[26] P. U. E. Onyisi *et al.* (CLEO Collaboration), Phys. Rev. D **79**, 052002 (2009).
[27] B. I. Eisenstein *et al.* (CLEO Collaboration), Phys. Rev. D **78**, 052003 (2008).
[28] D. Becirevic and A. B. Kaidalov, Phys. Lett. B **478**, 417 (2000).
[29] J. M. Link *et al.* (FOCUS Collaboration), Phys. Lett. B **621**, 72 (2005).
[30] S. Fajfer and J. F. Kamenik, Phys. Rev. D **71**, 014020 (2005).
[31] B. Aubert *et al.* (*BABAR* Collaboration), Phys. Rev. D **78**, 051101 (2008).
[32] M. Ablikim *et al.* (BES Collaboration), Phys. Rev. D **72**, 092002 (2005).